J Digit Imaging (2013) 26:1131–1140
DOI 10.1007/s10278-013-9601-z

Improvement of Partial Volume Segmentation for Brain Tissue on Diffusion Tensor Images Using Multiple-Tensor Estimation

Seiji Kumazawa · Takashi Yoshiura · Hiroshi Honda · Fukai Toyofuku

Published online: 16 April 2013

Abstract To improve evaluations of cortical and subcortical diffusivity in neurological diseases, it is necessary to improve the accuracy of brain diffusion tensor imaging (DTI) data segmentation. The conventional partial volume segmentation method fails to classify voxels with multiple white matter (WM) fiber orientations such as fiber-crossing regions. Our purpose was to improve the performance of segmentation by taking into account the partial volume effects due to both multiple tissue types and multiple WM fiber orientations. We quantitatively evaluated the overall performance of the proposed method using digital DTI phantom data. Moreover, we applied our method to human DTI data, and compared our results with those of a conventional method. In the phantom experiments, the conventional method and proposed method yielded almost the same root mean square error (RMSE) for gray matter (GM) and cerebrospinal fluid (CSF), while the RMSE in the proposed method was smaller than that in the conventional method for WM. The volume overlap measures between our segmentation results and the ground truth of the digital phantom were more than 0.8 in all three tissue types, and were greater than those in the conventional method. In visual comparisons for human data, the WM/GM/CSF regions obtained using our method were in better agreement with the corresponding regions depicted in the structural image than those obtained using the conventional method. The results of the digital phantom experiment and human data demonstrated that our method improved accuracy in the segmentation of brain tissue data on DTI compared to the conventional method.

S. Kumazawa (✉) · F. Toyofuku
Department of Health Sciences, Faculty of Medical Sciences, Kyushu University, 3-1-1, Maidashi, Higashi-ku, Fukuoka 812-8582, Japan
e-mail: s_kmzw@hs.med.kyushu-u.ac.jp

T. Yoshiura · H. Honda
Department of Clinical Radiology, Graduate School of Medical Sciences, Kyushu University, Fukuoka, Japan

Keywords DTI · Brain tissue segmentation · Digital DTI phantom · Partial volume effect · Multiple-tensor estimation

Introduction

Diffusion tensor imaging (DTI) measures the diffusion displacement properties of water, and provides a series of maps that reflect the different characteristics of the diffusion properties in different brain tissues [1, 2]. Maps derived from the DTI data are utilized for detecting gray matter (GM) and white matter (WM) microstructural abnormalities in neurodegenerative diseases such as Alzheimer's disease [3–8].

Recently, in order to study the cortical and subcortical diffusivity in neurological and neurodegenerative diseases, a few methods of brain tissue segmentation using DTI data have been proposed [9–12]. Some approaches utilize the registration with structural magnetic resonance image (MRI) (e.g. a T_1-weighted image) segmented into WM, GM and cerebrospinal fluid (CSF) regions [9, 10]. However, due to the imperfect registration between structural MRI and DTI, these methods suffer from misclassification of the voxels, which may result in erroneous interpretation of the DTI data [9, 10]. These misclassified voxels may lead to misinterpretation of the diffusion property when analyzing the diffusivity in a tissue from a neurodegenerative disease. In particular, CSF voxels erroneously assigned to the GM region by misregistration due to geometric distortion in echo planar imaging may result in significant deviation of the measured apparent diffusion coefficient (ADC) value in the GM region [9, 10]. Another approach is based on a Hidden Markov Random Field model and the Expectation-Maximization (HMRF-EM) algorithm [11]. This method can classify each voxel as a unique tissue type (categorized as a hard segmentation method) in the DTI space without the need for any registration. Since the current voxel size of DTI data is approximately 2 mm, the accuracy of the hard

segmentation approach is limited by partial volume effects [12, 13]. To avoid both these problems, the partial volume segmentation method has been proposed, which conducts brain tissue segmentation in DTI space without any registration, and estimates the partial volume fractions of tissue types within a voxel [12]. However, in DTI data, the partial volume effects within the voxel derive not only from the presence of multiple tissue types, but also from the presence of multiple WM fiber orientations. It is known that the presence of multiple WM fiber orientations such as fiber-crossing and fiber-branching regions results in low fractional anisotropy (FA) values for WM voxels due to the partial volume effect [14]. Because this method does not take into account the partial volume effect due to multiple WM fiber orientations, WM voxels with fiber-crossing and/or fiber-branching regions tend to be misclassified as GM.

To improve evaluations of cortical and subcortical diffusivity in neurological diseases using clinical DTI data, it is necessary to improve the accuracy of brain DTI data segmentation. A number of methods have been proposed to deal with the problem of partial volume averaging of the multiple fiber orientations in DTI tractography methods [15–19]. Instead of DTI data, some approaches are based on high angular resolution diffusion imaging (HARDI) data, which estimates the multiple fiber orientations within a single voxel [20]. Because HARDI requires the application of a number of gradient orientations (e.g., in one study [20], 126 diffusion gradient orientations were applied, resulting in a total scan time of 40 min), it is difficult to use in routine clinical practice. Other approaches based on DTI data are multiple tensor fitting techniques, which decompose the partial volume-averaged tensor to multiple tensors within the same voxel [18, 19, 21]. These methods can be applied to the DTI data acquired by clinical magnetic resonance (MR) sequences.

In this paper, we propose a partial volume DTI segmentation method to improve segmentation performance in the presence of multiple WM fiber orientations. In the proposed method, which uses multiple-tensor estimation, we take into account the partial volume effects due to both multiple tissue types, which were used in conventional method, and multiple WM fiber orientations. In this study, our aim was to develop the segmentation method for DTI data acquired by clinical MR sequence which does not require high *b* values. In order to evaluate the performance of our method, we compared its results with those of the conventional method using both a digital DTI phantom and human DTI data.

Materials and Methods

Partial Volume Segmentation for Multiple Tissue Types

First, we will describe briefly the conventional partial volume segmentation for multiple tissue types. The maps of three eigenvalues (λ_1, λ_2, and λ_3), ADC, and FA are used to estimate the partial volume fractions of WM, GM, and CSF in each voxel. Let $Y=[y_{11}, y_{21}, \ldots, y_{N1}, y_{12}, \ldots, y_{ij}, \ldots, y_{NL}]^{\mathrm{T}}$ be the obtained map, and y_{ij} denote the intensity at voxel i of map j ($1\le i\le N$, $1\le j\le L$, where N is the number of voxels and L is the total number of maps, i.e., $L=5$ in this study). Let $M=[m_{i1}, m_{i2}, .. m_{ik} .., m_{iK}]^{\mathrm{T}}$ be the partial volume fraction, and m_{ik} denotes the fraction of tissue type k within voxel i, where K is the number of tissues, $\sum_{k=1}^{K} m_{ik} = 1$, $0\le m_{ik}\le 1$. Let Φ be a model parameter set of the tissue class in the obtained map Y. Assuming that the partial volume fraction M and the tissue class parameter set Φ are independent, the posterior distribution of M and Φ given the obtained map Y is expressed as

$$P(M,\Phi|Y) = \frac{P(Y|M,\Phi)P(M)P(\Phi)}{P(Y)} \propto P(Y|M,\Phi)P(M)P(\Phi) \tag{1}$$

By taking the logarithm of Eq. 1, the likelihood energy function U(M, $\Phi|Y$) is given by

$$U(M,\Phi|Y) \propto U(Y|M,\Phi) + U(M) + U(\Phi), \tag{2}$$

where U($Y|M$, Φ) is the likelihood energy function of the obtained map Y, and U(M) and $U(\Phi)$ are the prior energy functions of the partial volume fraction M and tissue class parameter set Φ, respectively. By minimizing the likelihood energy function $U(M, \Phi|Y)$ instead of maximizing the posterior distribution $P(M, \Phi|Y)$, we can estimate the partial volume fraction M using the maximum a posteriori (MAP) approach. The posterior energy function U is given by

$$U = \sum_{j=1}^{L}\sum_{i=1}^{N}\sum_{k=1}^{K} m_{ik}^2 \left\|y_{ij} - v_{jk}\right\|^2 + \alpha \sum_{i=1}^{N}\sum_{k=1}^{K}\sum_{r\in N_i} \kappa_r \|m_{ik} - m_{rk}\|^2 + \sum_{i=1}^{N} \beta_i \left(1 - \sum_{k=1}^{K} m_{ik}\right), \tag{3}$$

where N_i is the first-order neighborhood of voxel i, α is a fixed parameter, κ_r is a scaling factor reflecting the difference among different orders of neighbors in a Markov random field model, and β_i is a Lagrange multiplier under the condition of $\sum_{k=1}^{K} m_{ik} = 1$. Taking the partial derivative with respect to m_{ik} and setting the result to zero, we obtain

$$m_{ik} = \frac{\beta_i + 2\alpha \sum_{r\in N_i} \kappa_r m_{rk}}{2\sum_{j=1}^{L} ||y_{ij} - v_{jk}||^2 + 2\alpha \sum_{r\in N_i} \kappa_r}, \tag{4}$$

where β_i is found by substituting Eq. 4 into $\sum_{k=1}^{K} m_{ik} = 1$. The tissue segmentation is performed by assigning a tissue type to each voxel based on the largest partial volume fraction among WM, GM, and CSF contained within the voxel [12].

Multiple-Tensor Estimation for Multiple WM Fiber Orientations

In the conventional method, WM voxels with multiple fiber orientations tend to be misclassified as GM because of their low FA values, a consequence of the partial volume effect of the diffusion tensors. In general, the WM fiber-crossing and fiber-branching voxels are adjacent to WM voxels. Therefore, we assumed that the WM voxels with multiple fiber orientations misclassified into the GM region by partial volume segmentation would be adjacent to the WM voxels. After extracting the voxels adjacent to WM voxels from the GM region, we applied multiple-tensor estimation to these voxels.

For the WM voxels with multiple fiber orientations, multiple-tensor estimation is used to decompose the partial volume-averaged tensor to multiple tensors in different multiple fiber compartments within the same voxel [20]. In a diffusion-weighted MR image, the observed MR signal S_i from a single diffusion compartment is given by

$$S_i = S_0 \exp\left(-b\boldsymbol{g}_i^{\mathrm{T}}\boldsymbol{D}\boldsymbol{g}_i\right), \tag{5}$$

where b is the b value, S_0 is the signal intensity with $b=0$ s/mm^2, i.e., the signal intensity of the non-diffusion weighted image, $\boldsymbol{g}_i$ is the unit vector of the ith diffusion encoding gradient, and $\boldsymbol{D}$ is the diffusion tensor [22]. Under some assumptions [14, 20], the observed signal in the presence of multiple fiber orientations is expressed as a finite mixture of n compartments:

$$S_i = S_0 \sum_{j=1}^{n} f_j \exp\left(-b\boldsymbol{g}_i^{\mathrm{T}}\boldsymbol{D}_j\boldsymbol{g}_i\right), \tag{6}$$

where f_j is the apparent volume fraction of the voxel with diffusion tensor $\boldsymbol{D}_j$. In this multiple tensor model, it is assumed that voxels contain one tissue type, i.e., WM only. Therefore, in Eq. 6, the S_0 of each compartment is the same. However, in our method, we assumed that each compartment contains either WM or GM, i.e., S_0 is different from compartment to compartment. Thus, Eq. 5 is rewritten as follows:

$$S_i = \sum_{j=1}^{n} f_j S_{0,j} \exp\left(-b\boldsymbol{g}_i^{\mathrm{T}}\mathbf{D}_j\boldsymbol{g}_i\right), \tag{7}$$

where $S_{0,j}$ is the component of the non-diffusion weighted image intensity in the jth compartment. In this study, we adopted a two-tensor model as found in the literature [18, 19, 21]:

$$S_i = fS_{0,1}\exp\left(-b\boldsymbol{g}_i^{\mathrm{T}}\boldsymbol{D}_1\boldsymbol{g}_i\right) + (1-f)S_{0,2}\exp\left(-b\boldsymbol{g}_i^{\mathrm{T}}\boldsymbol{D}_2\boldsymbol{g}_i\right). \tag{8}$$

In this model, we estimated the parameters, i.e., f, $S_{0,1}$, $S_{0,2}$, and the elements of tensors $\boldsymbol{D}_1$ and $\boldsymbol{D}_2$ for a given measured signal $\widehat{S}_i$ by minimizing the cost function. We define the cost function as follows:

$$C\left(f, S_{0,1}, S_{0,2}, \boldsymbol{D}_1, \boldsymbol{D}_2\right) = \sum_{i=1}^{l}\left(\frac{\widehat{S}_i - S_i}{S_i}\right)^2 + a\left(1 - \left|e_{1,2}\cdot e_{1,\mathrm{WM}}\right|\right), \tag{9}$$

where l is the number of diffusion encoding gradients. The first term of Eq. 9 represents the normalized square error, and the second term represents the smooth regularization constraint to ensure voxel-to-voxel coherence. We suppose that at least one diffusion tensor, $\boldsymbol{D}_2$, of the two tensors within a voxel, $\boldsymbol{D}_1$ and $\boldsymbol{D}_2$, is related to the diffusion tensor at the neighboring WM voxel. In order to reflect the continuous nature of fibers along neighboring WM voxels, we added the inner product between the principal eigenvector $\boldsymbol{e}_{1,2}$ of the tensor $\boldsymbol{D}_2$ and the principal eigenvector $\boldsymbol{e}_{1,\mathrm{WM}}$ of the neighboring WM voxel to the cost function. The variable a is a weighting factor, and was set to 0.1 in this study. A downhill simplex optimization method is used to minimize the cost function [23]. In order to avoid local minima in optimization, we used several different restart points (ten in this study) as described in the literature [20]. Initial values on each start point for the minimization were generated by using random values in the following way: the apparent volume fraction f was generated at random in the range from 0 to 1. $S_{0,2}$ was generated by adding the Gaussian random number with a standard deviation of 5 % of the S_0 to the measured S_0 at the neighboring WM voxel. $S_{0,1}$ was derived from $S_0 = fS_{0,1} + (1-f)S_{0,2}$. The elements of the tensor $\boldsymbol{D}_1$ were generated at random in the range from 10^{-4} to 10^{-5}. Each element of the tensor $\boldsymbol{D}_2$ was generated by adding the Gaussian random number with a standard deviation of 5 % to the corresponding element of the diffusion tensor at the neighboring WM voxel. Based on the tensors $\boldsymbol{D}_1$ and $\boldsymbol{D}_2$, the combination of the components in the voxels was checked to determine whether it was a WM–WM combination or not using a threshold of FA

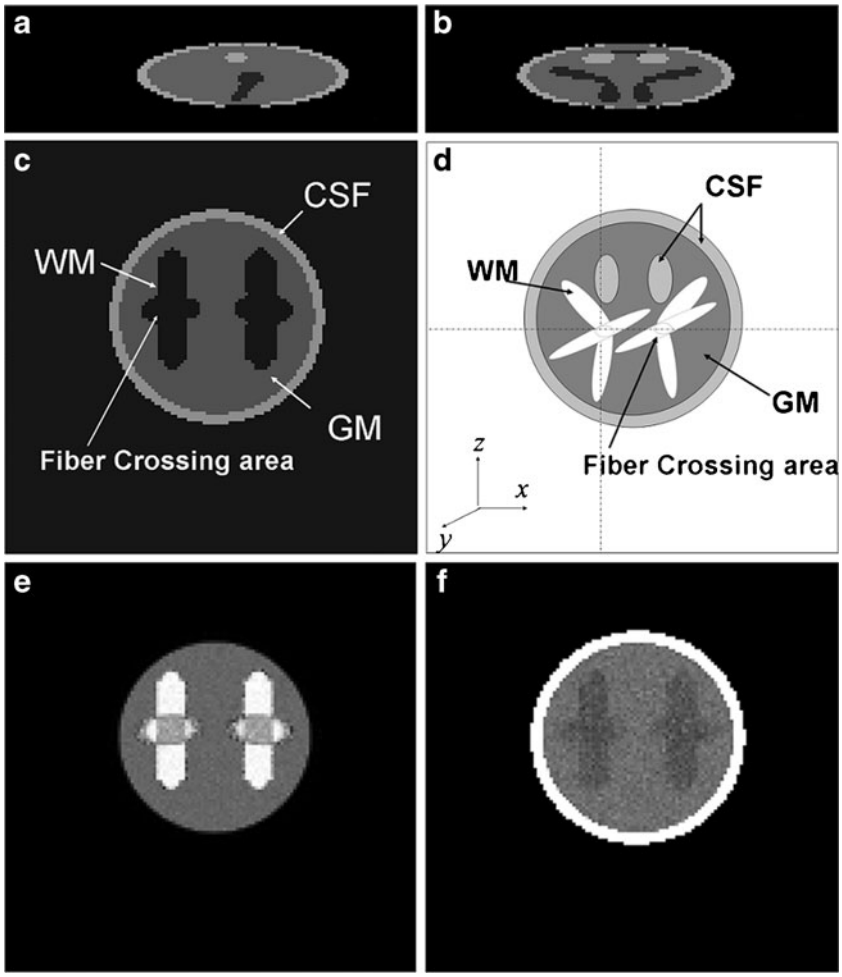

Fig. 1 Digital DTI phantom images: **a** sagittal view, **b** coronal view, and **c** axial view. **d** Schematic diagram of the phantom object in the object space. **a** and **c** Sagittal and axial cross sections along the *dotted lines* on panel **d**, respectively. **e** FA map, **f** ADC map, respectively

=0.25. In the case of WM–WM combinations, the diffusion tensor at the voxel of interest was replaced with the tensor having the higher FA value of the two tensors. Then, the partial volume fractions of WM, GM, and CSF in the voxel were recomputed based on Eqs. 3 and 4.

Digital DTI Phantom

For the design of the digital DTI phantom, we followed the description of a numerical phantom and the geometry of the tissue objects proposed by Alexander et al. [24]. Figure 1 shows the digital DTI phantom images (a, b, and c) used in this study, which were obtained by rendering the numerical phantom (d) in the object space.

Let $x_c \in R^3$ be the point in a continuous object space corresponding to the center of a voxel of the digital DTI phantom image, and $x_i \in N$ be a neighboring point of x_c, where N is the set of $5\times5\times5$ neighboring points within the voxel. The diffusion tensor of the tissue object in x_i is given by

$$D_{x_i} = \lambda_{1x_i} e_{1x_i} e_{1x_i}^t + \lambda_{2x_i} e_{2x_i} e_{2x_i}^t + \lambda_{3x_i} e_{3x_i} e_{3x_i}^t, \quad (10)$$

Table 1 Summary of the eigenvalues and the non-diffusion weighted image intensity, S_0, used to generate the simulated image intensities for each voxel in the digital DTI phantom data

	λ_1 [10^{-6} mm^2/s]	λ_2 [10^{-6} mm^2/s]	λ_3 [10^{-6} mm^2/s]	S_0
WM	N(1300,150)	N(550,40)	N(550,40)	N(200,100)
GM	N(1000,100)	N(800,60)	N(660,50)	N(270,14)
CSF	N(3200,100)	N(3200,100)	N(3200,100)	N(900,45)

These values were set in accordance with the literature, and were added to values generated at random from the Normal distribution. $N(a,b)$ indicates the normal distribution with mean a and standard deviation b

Table 2 The root mean square error (RMSE) between the true partial volume fraction and estimated partial volume fraction of each tissue type on the whole volume and on the slices including the maximum fiber-crossing area and single fiber area of the digital DTI phantom

	Whole volume			The slice including the maximum fiber-crossing area			The slice including the single fiber area		
	WM	GM	CSF	WM	GM	CSF	WM	GM	CSF
Conventional method	0.269	0.102	0.065	0.326	0.113	0.050	0.168	0.085	0.063
Proposed method	0.241	0.113	0.062	0.240	0.121	0.048	0.174	0.088	0.060

where λ_{1xi}, λ_{2x_i}, and λ_{3x_i} are eigenvalues of the object tissue in x_i, and $\boldsymbol{e}_{1xi}$, $\boldsymbol{e}_{2xi}$, and $\boldsymbol{e}_{3xi}$ are their corresponding eigenvectors. The simulated image intensity at a voxel in x_c is modeled by

$$S_{x_c} = \sum_{x_i \in N} \alpha S_0(x_i) \exp\left(-b\boldsymbol{g}^{\mathrm{T}} \boldsymbol{D}_{x_i} \boldsymbol{g}\right) + n, \tag{11}$$

where b is the b value, $S_0(x_i)$ is the non-diffusion weighted image intensity of the object tissue in x_i, $\boldsymbol{g}$ is the unit vector of the diffusion-encoding gradient, n is the Gaussian noise with a standard deviation of 5 % of the image intensity, α is a weighting factor, and i is a site within a voxel. In the fiber-crossing voxel, because the subsample point is included in two different objects of the WM fiber tract simultaneously, we decide which object to choose by random value. Figure 1e and f shows the FA map and ADC map, respectively. As shown in Fig. 1e, the WM fiber-crossing area in the FA map has low FA values due to the partial volume effect of the diffusion tensors: these FA values approach those in the GM area.

Table 1 shows the eigenvalues (10^{-6} mm^2/s) and S_0 of each tissue object; the eigenvalues were set in accordance with the literature [25], and were added to values generated at random from the Normal distribution. The other parameters in this phantom model were the same as the values and distributions described in the literature [24]. The synthetic DTI phantom data consisted of six diffusion-weighted image volumes (b=800 s/mm^2) and an unweighted image volume (b=0 s/mm^2) with a 128×128 in-plane resolution and 40 slices (field of view [FOV]: 230×230 mm^2, 3 mm thick). The voxel size was 1.8×1.8×3 mm^3, which is the same as that of the voxels used in our clinical data.

Evaluation on Digital DTI Phantom

Based on the known partial volume fractions of tissue types within a voxel in the ground truth data of the digital DTI phantom, we assessed the performance of our proposed method and the conventional method [12] in the estimation of the partial volume fractions. To investigate the estimation error rate of each tissue class, we used the root mean square error (RMSE) described in the literature [26]. The RMSE of the partial volume fraction of tissue type k is given by

$$\mathrm{RMSE} = \sqrt{\sum_{\mathrm{i}} \left(\widehat{m}_{ik} - m_{ik}\right)^2 / N}, \tag{12}$$

where m_{ik} and $\widehat{m}_{ik}$ are the true partial volume fraction and estimated partial volume fraction of the tissue type k within voxel i, respectively, and N is the number of voxels in which the partial volume fraction of tissue type k is nonzero in the ground truth data.

In further quantitative evaluation, we used the volume overlap measure between the segmentation result and the ground truth data, each voxel of which was assigned a tissue type label. The volume overlap measure used in this study is given by

Table 3 Volume overlaps between segmentation results and ground truth in each tissue type on the whole volume and on the slices including the maximum fiber-crossing area and single fiber area of the digital DTI phantom

	Whole volume			The slice including the maximum fiber-crossing area			The slice including the single fiber area		
	WM	GM	CSF	WM	GM	CSF	WM	GM	CSF
Conventional method	0.677	0.945	0.926	0.668	0.878	0.941	0.824	0.968	0.923
Proposed method	0.860	0.954	0.928	0.839	0.921	0.942	0.817	0.967	0.924

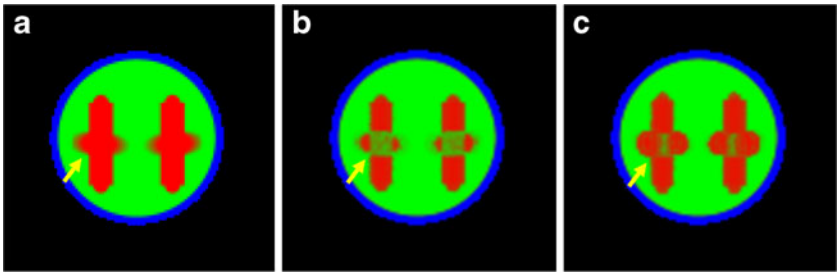

Fig. 2 Digital DTI phantom study. The maps of **a** the true partial volume fractions in the ground truth data, **b** partial volume fractions estimated by the conventional method, and **c** partial volume fractions estimated by proposed method. *Yellow arrows* point to fiber-crossing areas. Note that the partial volume fractions of WM, GM, and CSF in a voxel, which ranged from 0 to 1, are respectively assigned to *red*, *green*, and *blue components* in the color image, which ranged from 0 to 255

$$J(S,G) = \frac{|S \cap G|}{|S \cup G|}, \tag{13}$$

where S is the volume data of the segmented tissue image and G is the volume data of the same type tissue image in the ground truth data.

Human DTI Data

The use of the human data was approved by our Institutional Review Board. Written informed consent was obtained from the subjects. MR imaging was performed on a 1.5-Tesla clinical scanner (Magnetom Symphony, Siemens, Erlangen, Germany) with an eight-channel phased-array coil. For five healthy volunteers, DTI data covering the whole brain were acquired using a single-shot echo-planar imaging pulse sequence with repetition time (TR)=8,600 ms and echo time (TE)=119 ms. The DTI data consisted of diffusion-weighted image volumes acquired using a six-directional diffusion encoding scheme at a b value of 800 s/mm^2 and a non-diffusion weighted image volume (b=0 s/mm^2). Each volume had 40 axial slices with a 128×128 in-plane resolution (FOV: 230×230 mm^2, 3 mm thickness), and the resultant voxel size was 1.8×1.8×3.0 mm^3.

In addition, in order to compare the segmentation results with the structural images visually, T_1-weighted images of the same subject were obtained using an MPRAGE (magnetization prepared rapid gradient echo) sequence (TR=2,090 ms, TE=3.93 ms, inversion time [TI]=1,100 ms, flip angle=15°). Each slice had a 256×256 in-plane resolution (FOV: 230×230 mm^2, 1 mm thickness). These original images were converted into isotropic three-dimensional (3D) images with a voxel size of 0.898 mm. The resultant 3D volume data had 256×256×137–161 voxels.

We evaluated the brain tissue segmentation results by visual comparisons of the segmented regions with the structural images, because we did not have a ground truth in human DTI data.

Results

Digital DTI Phantom Studies

Table 2 shows the RMSE between the true partial volume fraction and the estimated partial volume fraction of each tissue type based on the whole volume and on the slices including the fiber-crossing area and single fiber area of the digital DTI phantom. Because only three out of 40 slices included the fiber-crossing area, we investigated the RMSE not only for the whole volume (40 slices) but also for the slice including the maximum area of fiber crossing. Whereas the RMSE of the conventional method and proposed method were almost the same for GM and CSF, the RMSE of the proposed method was smaller than that of the conventional method for WM in the slice including the maximum area of fiber crossing.

Fig. 3 Digital DTI phantom study. **a** The ground truth of hard segmentation, **b** segmentation result using the conventional method, and **c** segmentation result using proposed method

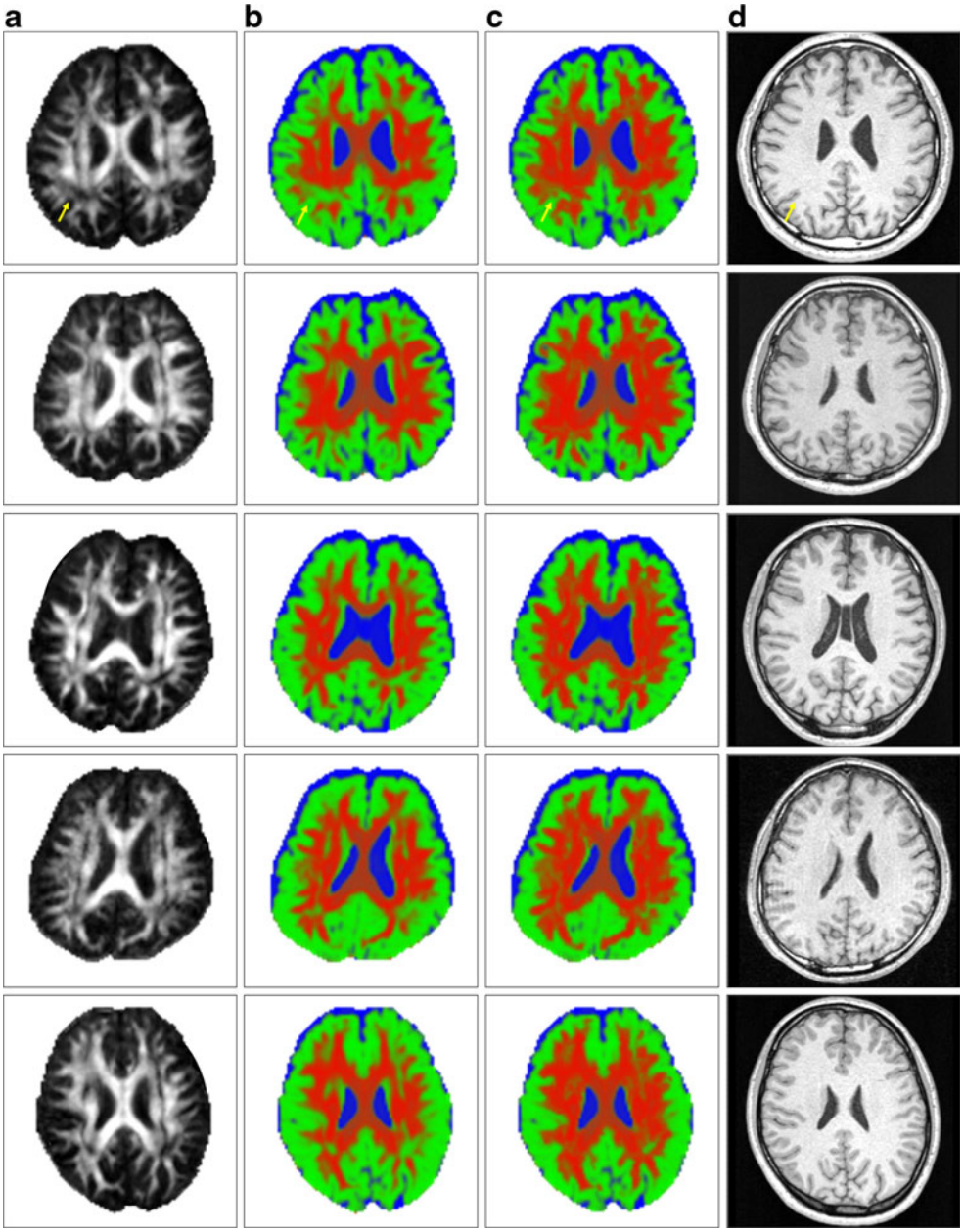

Fig. 4 Images in five healthy volunteers at the level of corona radiata, which include many voxels with more than one fiber orientation. **a** The FA maps, **b** the estimated partial volume fraction maps obtained by the conventional method, **c** the estimated partial volume fraction maps obtained by proposed method, and the structural images (T_1-weighted images). *Yellow arrows* point to the parietal deep WM area. Note that in panels **b** and **c**, the partial volume fractions of WM, GM, and CSF in the voxel, which ranged from 0 to 1, are respectively assigned to *red*, *green*, and *blue components* in the color image, which ranged from 0 to 255

Table 3 shows the volume overlaps between ground truth and segmentation results using the conventional method and our proposed method for each tissue type. In all three tissue types in the whole volume and the slices including the maximum area of fiber crossing and single fiber area, the values of volume overlap in the proposed method were more than 0.8. In WM in the axial slice including maximum area of fiber crossing, the value of volume overlap was improved from 0.668 to 0.839 by applying our multiple-tensor estimation. In WM region in the single fiber area, the values of volume overlap by the conventional method and proposed method were almost the same.

Figure 2a–c shows the maps of the true partial volume fractions in the ground truth data and estimated partial volume fractions by the conventional method and proposed method, respectively. These images correspond to the axial slice including the maximum area of fiber crossing (yellow arrow) as demonstrated in Tables 2 and 3. Figure 3a–c shows the ground truth of hard segmentation and segmentation results based on partial volume fractions using the conventional method and proposed method, respectively. Figures 2 and 3 show that WM fiber-crossing regions are misclassified into the GM region by the conventional method, but could be discriminated as WM by our proposed method.

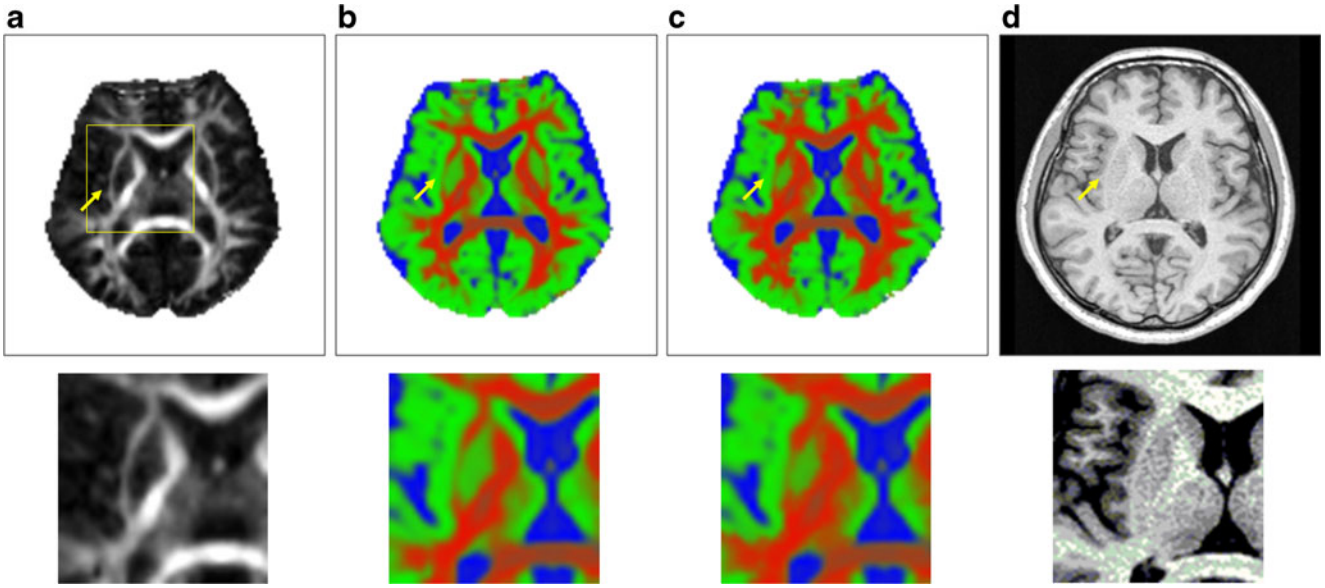

Fig. 5 Images (*top*) at the external capsule level and magnifications (*bottom*) of the region. **a** The FA maps, **b** the estimated partial volume fraction maps obtained by the conventional method, **c** the estimated partial volume fraction maps obtained by proposed method, and **d** the structural images (T_1-weighted images). *Yellow arrows* point to the external capsules

Human DTI Data Study

To assess the performance of our proposed method, we present the estimated partial volume fraction maps of the human DTI data, and compare them with the results using the conventional method. Figure 4 shows the results in five healthy volunteers, at the level of corona radiata, which includes many WM voxels with more than one fiber orientation as analyzed in the literature [15]. Columns (a), (b), (c) and (d) show the FA maps, the estimated partial volume fraction maps obtained by the conventional and proposed methods, and the structural images (T_1-weighted images), respectively. Figure 5 shows the example of the results at the external capsule level. The partial volume fractions of WM, GM, and CSF in a voxel, which ranged from 0 to 1, were respectively assigned to red, green and blue components in the color image, which ranged from 0 to 255.

Discussion

We evaluated the performance of the conventional method and proposed method quantitatively using digital DTI phantom data. As shown in Table 2, the RMSE in both methods were in the range between 0.048 and 0.326: these errors were comparable to those (range from 0.1 to 0.3) in the literature [26, 27]. However, it should be noted that a direct comparison cannot be made because the signal/noise ratio, image resolution and the phantom image were different from those used in the literature. We also assessed the performance of the two methods using the volume overlap measure. As shown in Table 3, although the performance of the segmentation in the fiber-crossing region was improved by applying the multiple-tensor estimation, some WM voxels were still depicted as GM in the center area of the fiber-crossing region (Fig. 3c). Our two-tensor estimation model utilizes the diffusion tensor of the neighboring WM voxel in Eqs. 8 and 9. By applying the proposed method to the WM crossing voxel, the diffusion tensor at the voxel was decomposed into the two diffusion tensors by minimizing the cost function in Eq. 9. Then, the multiple-tensor estimation was applied to the voxel adjacent to the new WM voxels estimated by the proposed method. By applying the proposed method iteratively in this manner, the estimation error might accumulate. Because our proposed method checks the voxel from the edge of the crossing area to the center, some voxels in the center area of the fiber-crossing region may not have been extracted as WM due to the accumulated error.

We applied the conventional method and proposed method to human DTI data, and assessed the brain tissue segmentation results visually because we did not have a ground truth in human data. Columns (b) and (c) in Figs. 4 and 5 show the results obtained by the two methods. Figure 4 shows the slice at the level of the corona radiata, which includes many WM voxels with more than one fiber orientation [15]. It is known that the WM voxels in fiber-crossing and/or fiber-branching regions tend to have low FA values due to the partial volume effect [14]. As shown in Fig. 4, the voxels in the parietal deep WM area have low FA values

(yellow arrow in Fig. 4a), but these voxels have image intensity corresponding to WM in the T_1-weighted images (yellow arrow in Fig. 4d). It seems that the conventional method tended to misclassify these WM voxels with low FA values as GM. As shown in column (c) of Fig. 4, the segmentation performance at these voxels was improved by applying the multiple-tensor estimation. The WM regions estimated by proposed method more closely simulated the WM regions depicted in the T_1 images than those estimated by the conventional method. Whereas the segmentation performance of the WM region is improved by applying the multiple-tensor estimation, WM region might be overestimated due to the aforementioned accumulated error. In our future work, we plan to perform quantitative evaluations or comparisons of both methods.

As demonstrated in the literature [12], the conventional partial volume segmentation method has several advantages over the hard segmentation method based on the HMRF-EM algorithm [11]. For example, the external capsules and the putamen were depicted by the conventional method as WM and GM, respectively, whereas it was difficult to identify the external capsules and the putamen using the HMRF-EM method. Figure 5 shows the results at the external capsule level. In visual comparisons, these structures are correctly identified by both methods (yellow arrows). Thus, our proposed method improved the segmentation performance in the WM fiber-crossing area, while maintaining similar segmentation accuracy in other areas. These results suggest that our proposed method, which takes into account the partial volume effects due to both multiple tissue types and multiple WM fiber orientations, was able to perform a reasonable segmentation of the brain tissue on DTI data. The improvement of the segmentation accuracy may reduce the risk of misinterpreting the diffusion property when studying the cortical and subcortical diffusivity in neurodegenerative disease.

In this paper, we consider the segmentation for DTI data acquired in routine clinical practice. However, recently the diffusion imaging techniques with more gradient orientations such as Q-ball imaging [28] and diffusion kurtosis imaging [29] are used in clinical [30]. The information provided by these imaging is used to improve WM fiber tractography [31]. In our future work, we plan to apply the conventional method and proposed method to these data. We will investigate the performance of these methods by using digital phantom data in terms of the number of gradient orientations and signal-to-noise ratio.

Conclusions

We have presented an extension of the conventional partial volume segmentation to improve the segmentation performance in fiber-crossing areas by applying multiple-tensor estimation. The proposed method takes into account the partial volume effects due to both multiple tissue types and multiple WM fiber orientations. The results of the digital DTI phantom experiment and human DTI data demonstrate that our method improves segmentation accuracy compared with the conventional method.

Acknowledgments This study was supported, in part, by a Grant-in-Aid from the Ministry of Education, Science and Culture of Japan (#23500561).

References

1. Brunberg JA, Chenevert TL, McKeever PE, et al: In vivo MR determination of water diffusion coefficients and diffusion anisotropy: correlation with structural alteration in gliomas of the cerebral hemispheres. AJNR Am J Neuroradiol 16 (2):361–71, 1995
2. Chien D, Kwong KK, Gress DR, et al: MR diffusion imaging of cerebral infarction in humans. AJNR Am J Neuroradiol 13 (4):1097–105, 1992
3. Stahl R, Dietrich O, Teipel S, et al: Assessment of axonal degeneration on Alzheimer's disease with diffusion tensor MRI. Radiologe 43:566–575, 2003
4. Horsfield MA, Jones DK: Applications of diffusion-weighted and diffusion tensor MRI to white matter diseases — a review. NMR Biomed 15(7–8):570–577, 2002
5. Hanyu H, Shindo H, Kakizaki D, et al: Increased water diffusion in cerebral white matter in Alzheimer's disease. Gerontology 43 (6):343–51, 1997
6. Yoshiura T, Mihara F, Ogomori K, et al: Diffusion tensor in posterior cingulate gyrus: correlation with cognitive decline in Alzheimer's disease. Neuroreport 13(17):2299–302, 2002
7. Kantarci K, Jack Jr, CR, Xu YC, et al: Mild cognitive impairment and Alzheimer disease: regional diffusivity of water. Radiology 219(1):101–7, 2001
8. Bozzali M, Falini A, Franceschi M, et al: White matter damage in Alzheimer's disease assessed in vivo using diffusion tensor magnetic resonance imaging. J Neurol Neurosurg Psychiatry 72 (6):742–746, 2002
9. Yoshiura T, Mihara F, Tanaka A, et al: Novel method to estimate and display cerebral cortical degeneration using diffusion-weighted magnetic resonance imaging. Magn Reson Med 54 (2):455–459, 2005
10. Liu T, Young G, Huang L, et al: 76-Space analysis of grey matter diffusivity: methods and applications. NeuroImage 31(1):51–65, 2006
11. Liu T, Li H, Wong K, et al: Brain tissue segmentation based on DTI data. Neuroimage 38(1):114–23, 2007
12. Kumazawa S, Yoshiura T, Honda H, et al: Partial volume estimation and segmentation of brain tissue based on diffusion tensor MRI. Med Phys 37(4):1482–90, 2010
13. Van Leemput K, Maes F, Vandermeulen D, et al: A unifying framework for partial volume segmentation of brain MR images. IEEE Trans Med Imaging 22(1):105–19, 2003
14. Alexander AL, Hasan KM, Lazar M, et al: Analysis of partial volume effects in diffusion-tensor MRI. Magn Reson Med 45 (5):770–80, 2001
15. Behrens TE, Berg HJ, Jbabdi S, et al: Probabilistic diffusion tractography with multiple fibre orientations: what can we gain? Neuroimage 34(1):144–55, 2007

16. Campbell JS, Siddiqi K, Rymar VV, et al: Flow-based fiber tracking with diffusion tensor and q-ball data: validation and comparison to principal diffusion direction techniques. Neuroimage 27(4):725–36, 2005
17. Kumazawa S, Yoshiura T, Arimura H, et al: Estimation of white matter connectivity based on a three-dimensional directional diffusion function in diffusion tensor MRI. Med Phys 33(12):4643–52, 2006
18. Pasternak O, Assaf Y, Intrator N, et al: Variational multiple-tensor fitting of fiber-ambiguous diffusion-weighted magnetic resonance imaging voxels. Magn Reson Imaging 26(8):1133–44, 2008
19. Ramirez-Manzanares A, Rivera M: Basis tensor decomposition for restoring intra-voxel structure and stochastic walks for inferring brain connectivity in DT-MRI. International Journal of Computer Vision 69(1):77–92, 2006
20. Tuch DS, Reese TG, Wiegell MR, et al: High angular resolution diffusion imaging reveals intravoxel white matter fiber heterogeneity. Magn Reson Med 48(4):577–82, 2002
21. Sotiropoulos SN, Bai L, Morgan PS, et al: A regularized two-tensor model fit to low angular resolution diffusion images using basis directions. J Magn Reson Imaging 28(1):199–209, 2008
22. Basser PJ, Mattiello J, LeBihan D: Estimation of the effective self-diffusion tensor from the NMR spin echo. J Magn Reson B 103 (3):247–254, 1994
23. Press WH, Teukolsky SA, Vetterling WT, et al: Numerical Recipes in C. The Art of Scientific Computing. Cambridge Univ. Press, New York, 1998
24. Alexander DC, Pierpaoli C, Basser PJ, et al: Techniques for spatial normalization of diffusion tensor images. Proc. SPIE 3979:470–481, 2000
25. Pierpaoli C, Jezzard P, Basser PJ, et al: Diffusion tensor MR imaging of the human brain. Radiology 201(3):637–48, 1996
26. Choi HS, Haynor DR, Kim Y: Partial volume tissue classification of multichannel magnetic resonance images—a mixel model. IEEE Trans Med Imaging 10(3):395–407, 1991
27. Shattuck DW, Sandor-Leahy SR, Schaper KA, et al: Magnetic resonance image tissue classification using a partial volume model. Neuroimage 13(5):856–76, 2001
28. Tuch DS: Q-ball imaging. Magn Reson Med 52(6):1358–72, 2004
29. Jensen JH, Helpern JA, Ramani A, et al: Diffusional kurtosis imaging: the quantification of non-gaussian water diffusion by means of magnetic resonance imaging. Magn Reson Med 53 (6):1432–40, 2005
30. Wang JJ, Lin WY, Lu CS, et al: Parkinson disease: diagnostic utility of diffusion kurtosis imaging. Radiology 261(1):210–7, 2011
31. Lazar M, Jensen JH, Xuan L, et al: Estimation of the orientation distribution function from diffusional kurtosis imaging. Magn Reson Med 60(4):774–781, 2008